Ultrasmall α-MnO_2 with Low Aspect Ratio: Applications to Electrochemical Multivalent-Ion Intercalation Hosts and Aerobic Oxidation Catalysts

*Reona Iimura, Shiori Kawasaki, Takashi Yabu, Shinnosuke Tachibana, Kazuya Yamaguchi, Toshihiko Mandai, Kazuaki Kisu, Naoto Kitamura, Zhirong Zhao-Karger, Shin-ichi Orimo, Yasushi Idemoto, Masaki Matsui, Maximilian Fichtner, Itaru Honma, Tetsu Ichitsubo, and Hiroaki Kobayashi**

Hollandite-type α-MnO_2 exhibits exceptional promise in current industrial applications and in advancing next-generation green energy technologies, such as multivalent (Mg^{2+}, Ca^{2+}, and Zn^{2+}) ion battery cathodes and aerobic oxidation catalysts. Considering the slow diffusion of multivalent cations within α-MnO_2 tunnels and the catalytic activity at edge surfaces, ultrasmall α-MnO_2 particles with a lower aspect ratio are expected to unlock the full potential. In this study, ultrasmall α-MnO_2 (<10 nm) with a low aspect ratio ($c/a \approx 2$) is synthesized using a newly developed alcohol solution process. This material demonstrates exceptional performance across various multivalent battery systems, primarily due to the significantly reduced cation diffusion distance. Notably, an ultrasmall α-MnO_2-graphene composite achieves high capacity with low overpotential when paired with an F-free electrolyte in Ca battery. Regarding aerobic oxidation catalysis, the nanosizing of α-MnO_2 has a profound impact on aerobic oxidation catalysis. The increased efficiency of oxidative conversion reactions, such as the oxidation of 1-phenylethanol, is attributed to the greatly expanded active surface area of the catalyst. The versatile functionality of ultrasmall α-MnO_2 underscores its potential to revolutionize energy storage and catalysis, offering broad applicability in next-generation green energy technologies.

1. Introduction

Owing to its numerous advantages toward industrial use, manganese dioxides (MnO_2) have attracted significant attention as promising functional materials.[1] MnO_2 possesses a diverse range of crystalline structures with multiple valence states (Mn^{2+}, Mn^{3+}, and Mn^{4+}),[2] where MnO_6 octahedral units are arranged in various configurations influenced by the presence of other cations and the thermodynamic conditions during crystallization.[3] This diversity results in a wide selection of crystal structures, including α (hollandite),[4] β (pyrolusite),[5] R (ramsdellite),[6] γ (a mixture of β and R),[7] δ (birnessite),[8] and λ (defect spinel),[9] each possessing distinct physical and chemical properties. Among various crystal structures, the hollandite-type (α-type) stands out as a commonly utilized high-performance material with versatile applications, such as cathode for energy

R. Iimura, S. Kawasaki, S. Tachibana, I. Honma, H. Kobayashi
Institute of Multidisciplinary Research for Advanced Materials (IMRAM)
Tohoku University
Sendai 980–8577, Japan

R. Iimura, Z. Zhao-Karger, M. Fichtner
Institute of Nanotechnology (INT)
Karlsruhe Institute of Technology (KIT)
76344 Karlsruhe, Germany

R. Iimura, Z. Zhao-Karger, M. Fichtner
Helmholtz Institute Ulm (HIU)
89081 Ulm, Germany

T. Yabu, M. Matsui, H. Kobayashi
Department of Chemistry
Faculty of Science
Hokkaido University
Sapporo 060–0810, Japan
E-mail: h.kobayashi@sci.hokudai.ac.jp

K. Yamaguchi
Department of Applied Chemistry
School of Engineering
The University of Tokyo
Tokyo 113–8656, Japan

T. Mandai
Center for Green Research on Energy and Environmental Materials
National Institute for Materials Science (NIMS)
Tsukuba 305-0044, Japan

K. Kisu, S.-ichi Orimo, T. Ichitsubo
Institute for Materials Research (IMR)
Tohoku University
Sendai 980–8577, Japan

K. Kisu
College of Engineering
Shibaura Institute of Technology
Tokyo 135–8548, Japan

N. Kitamura, Y. Idemoto
Faculty of Science & Technology
Tokyo University of Science
Noda 278–8510, Japan

storage,[10] aerobic oxidation catalysis,[11] sensing materials,[12] and absorbents.[13]

In the electrode applications, α-MnO_2 has been deeply investigated as a cathode for monovalent cation intercalation host (Li^+, Na^+, and K^+).[10a,14] However, the host structure tends to be distorted and collapsed after a large amount of cation insertion;[15] its application has been limited to the primary battery.[16] These days, the potential use of α-MnO_2 cathode toward multivalent cation (Mg^{2+}, Ca^{2+}, and Zn^{2+}) battery systems, possessing cost-effectiveness and high-energy density, have been extensively investigated, since the amount of cations required is halved compared with the monovalent battery systems, enabling the reversibility of α-MnO_2 cathode.[17] In addition, the redox cycling of Mn^{4+}/Mn^{3+} ions occurs at high voltage,[18] which can compensate for the disadvantage of lower reduction potential (Ca; –2.89 V, Mg; –2.36 V, and Zn; –0.763 V) compared to Li.[19] Indeed, previous studies have indicated that α-type materials are relatively suitable for cathode materials capable of reversible magnesium intercalation.[3d] Moreover, many researchers focus on zinc battery systems because of the superior performance in aqueous electrolytes,[20] demonstrating impressive capacity retention and high-rate capabilities.[21]

In the field of catalysis, α-MnO_2 exhibits great potential as an eco-friendly aerobic oxidation catalyst in various oxidative functional group transformations[11,22] because it can oxidize a variety of substrates by the Mars-van Krevelen mechanism, which directly utilizes its lattice oxygen, or by the one-electron transfer (SET) oxidation mechanism. This approach eliminates the demand for hazardous reagents and the generation of substantial quantities of inorganic by-products, thereby paving the way for environmentally responsible synthesis.

In both electrode and catalyst applications, a key to unlocking the full potential of α-MnO_2 lies in nanoparticulation, but simply reducing particle size is not sufficient. Considering multivalent cations diffuse in the direction of the tunnel much slower than monovalent cations, and catalysts show high activity on the edge of tunnels, achieving a lower aspect ratio (c/a), having low cation diffusion distance and many edge surfaces, holds considerable potential for enhancing material performance significantly. Moreover, α-MnO_2 involves cations like K^+, NH_4^+, and Ag^+ to maintain the tunnel structure;[14b,23] the type and the amount of introduced cations should affect the host capability. To harness the full potential of α-MnO_2 as an electrode material, a removable guest cation, i.e., NH_4^+ is the most promising choice. To date, numerous attempts have been made to achieve nanoparticulation of α-MnO_2 through a wide range of metal-doping.[11a,14b,24] While their approaches have successfully led to an increase in the specific surface area, the doped metal is likely to enter the guest site of the tunnel structure and distort the structure significantly, which might compromise the host capability as the cathode. Therefore, nanoparticulation techniques without metal doping are required.

S.-ichi Orimo
Advanced Institute for Materials Research (WPI-AIMR)
Tohoku University
Sendai 980–8577, Japan

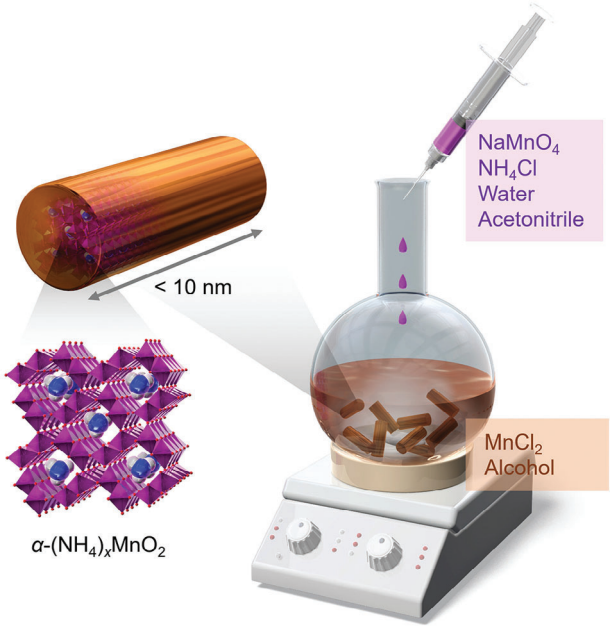

Figure 1. Schematic illustration of ultrasmall α-MnO_2 synthesis.

Typically, α-MnO_2 is synthesized using a hydrothermal approach, which has a challenge toward nanoparticulation, since the dissolution and recrystallization of the nucleus easily occur during synthesis. Here, we have innovatively combined our extensively reported alcohol reduction method for Mn-based spinel/todorokite/buserite synthesis[25] and the conventional hydrothermal approach,[3a,8a] enabling the nanoparticulation of α-MnO_2. Our developed alcohol solution process, devoid of any calcination steps, successfully produces ultrasmall α-MnO_2 particles (<10 nm) with a low aspect ratio ($c/a \sim 2$). Thus obtained ultrasmall α-MnO_2 shows a superior performance both in multivalent battery cathode and aerobic oxidation catalyst.

2. Results and Discussion

2.1. Synthesis and Characterization of Ultrasmall α-MnO_2

Figure 1 illustrates the alcohol solution process of ultrasmall α-MnO_2 synthesis. In the process, alcohol is just a solvent that suppresses the dissolution and recrystallization of oxides, and α-MnO_2 is synthesized by the redox reaction of Mn^{7+} (permanganate MnO_4^-) and Mn^{2+} in primary (*n*-PrOH, EtOH, or MeOH; PrOH: propanol, EtOH: ethanol, MeOH: methanol) or secondary (*i*-PrOH) alcohol solution. Note that $NaMnO_4$ was used as a permanganate salt in this work instead of the generally used $KMnO_4$, since $NaMnO_4$ has higher solubility in an organic solvent compared to $KMnO_4$.[26] Additionally, sodium-containing manganese oxides usually form a layered structure;[8a] they serve as precursors for various tunnel-type manganese oxides containing α-MnO_2.[3a] On the other hand, the permanganate should react with alcohol rapidly. Therefore, $NaMnO_4$ was dissolved in acetonitrile (stable against oxidation) to prepare a precursor solution. In the precursor solution, water and NH_4Cl were added for nucleation of α-MnO_2. This precursor solution was then added

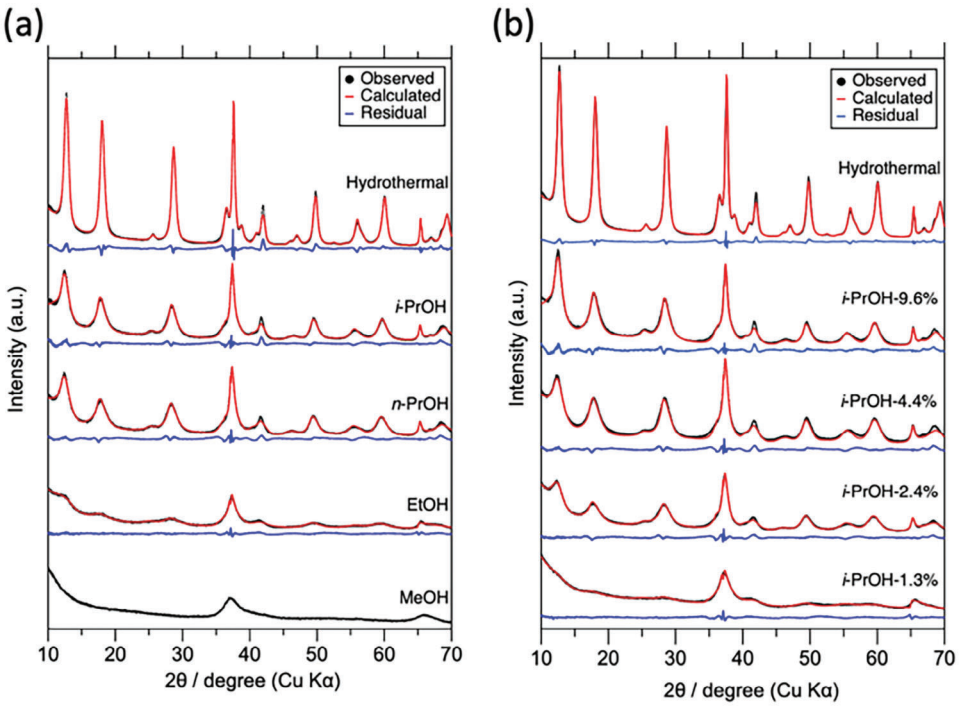

Figure 2. α-MnO_2 XRD patterns with fitting curves by Rietveld refinement with differences of a) alcohol solvent and b) differences of water content in *i*-PrOH reaction solution.

dropwise to an alcohol solution containing $MnCl_2$. A brown precipitate promptly formed, followed by refluxing for an hour to obtain ultrasmall α-MnO_2.

Figure 2a shows X-ray diffraction (XRD) patterns of α-MnO_2 synthesized via the hydrothermal process (α-MnO_2-hydro) and the alcohol solution process with different alcohol solvents (α-MnO_2-*i*-PrOH, α-MnO_2-*n*-PrOH, α-MnO_2-EtOH, and α-MnO_2-MeOH). All the XRD patterns, except α-MnO_2-MeOH, well-matched the single-phase of tetragonal α-MnO_2 with the $I4/m$ space group through Rietveld refinements (Table S1, Supporting Information).[27] Compared with XRD patterns of α-MnO_2-hydro, α-MnO_2 synthesized via the alcohol solution process presented markedly broad XRD patterns, suggesting the formation of nanoparticles. The variation in particle size can be attributed to variations in the dielectric constant of the alcohol solvent, as well as disparities in reflux temperatures. For instance, comparing α-MnO_2-*i*-PrOH to α-MnO_2-EtOH having a similar reflux temperature, EtOH has the higher polarity, strengthening the hydrogen bonds with the permanganate anion. Consequently, this lowers the activation energy required for α-MnO_2 nucleation, favoring nucleation over the growth of larger α-MnO_2 particles. This is in line with a previous report on δ-MnO_2 nanoparticle formation.[28]

Figure 2b displays the XRD pattern of α-MnO_2, illustrating the influence of varying water contents in the synthesis process. Samples were labeled as α-MnO_2-*i*-PrOH-x (x is the volume ratio of H_2O/(*i*-PrOH+H_2O)) to clarify the amount of H_2O in the reaction solvent. As well as Figure 2a, all the XRD patterns well-matched the single-phase of tetragonal α-MnO_2 through Rietveld refinements (Table S1, Supporting Information). Moreover, the selected area electron diffraction (SAED) analysis of α-MnO_2-hydro, α-MnO_2-*i*-PrOH-2.4%, and α-MnO_2-*i*-PrOH−1.3% shown in Figure S1a–c (Supporting Information) reveals the diffraction rings correlating to the obtained XRD pattern, supporting the formation of α-MnO_2. To further investigate the crystalline phase of the α-MnO_2, a pair distribution function (PDF) analysis using X-ray total scattering data (Figure S2, Supporting Information) was conducted.[29,30] The total correlation function $T(r)$ of the α-MnO_2-*i*-PrOH−1.3% and α-MnO_2-EtOH clearly shows both edge-shared and corner-shared Mn-Mn peaks. However, α-MnO_2-MeOH exhibits a weak and broad peak of corner-shared Mn-Mn, suggesting the existence of both tunnel and layered phases.

As the water content decreases, the XRD patterns become broader (Figure 2b), indicating the downsizing of nanoparticles, also supported by the Rietveld refinement (Table S1, Supporting Information). A large specific surface area (SSA) of more than 150 $m^2\ g^{-1}$ supports the nanoparticulation (Table S2, Supporting Information); the SSA of hydrothermally synthesized α-MnO_2 is typically 70–100 $m^2\ g^{-1}$.[23a] **Figure 3** presents high-resolution transmission electron microscopy (HR-TEM) images of α-MnO_2-hydro, α-MnO_2-*i*-PrOH-2.4%, and α-MnO_2-*i*-PrOH−1.3%. The low-magnified images are shown in Figure S1c–i (Supporting Information). In all the samples, clear lattice fringes were observed with evenly spaced intervals, indicating the formation of α-MnO_2 crystals. Additionally, primary particles of α-MnO_2 synthesized through the alcohol solution process underwent significant nanoparticulation, as summarized in Figure 3d. By adjusting the water content in the reaction solution, not only the particle size but also the aspect ratio (c/a) changed significantly. Interestingly, α-MnO_2-EtOH exhibited a needle-like particle morphology with a longer c-axis direction and a larger aspect ratio shown in Figure S3 (Supporting Information), though

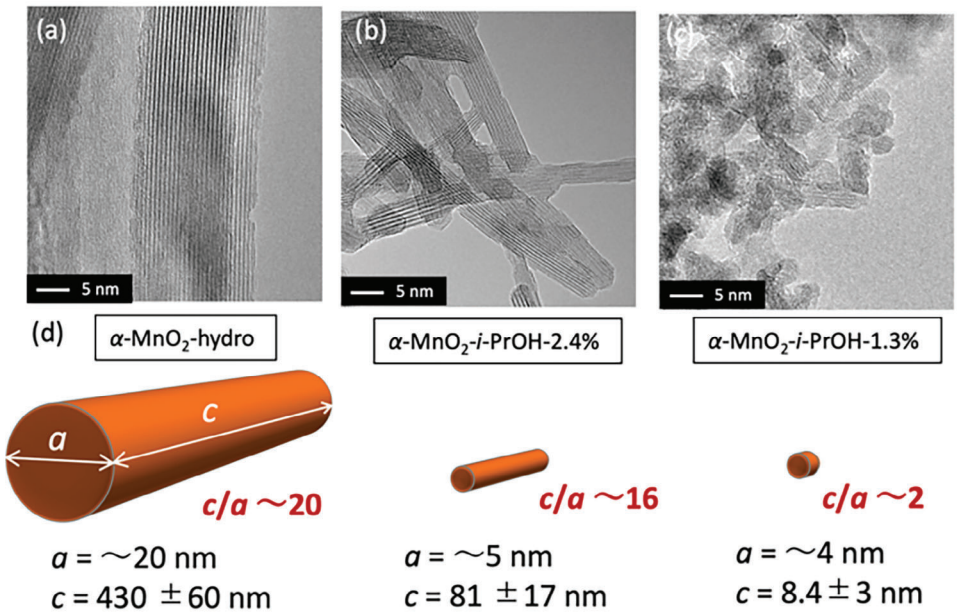

Figure 3. HR-TEM images of a) α-MnO_2-hydro, b) α-MnO_2-*i*-PrOH-2.4%, c) α-MnO_2-*i*-PrOH−1.3%. d) Summary of *a* and *c* axis length for each α-MnO_2 particle.

it shows a similar XRD pattern shape and lattice constants to α-MnO_2-*i*-PrOH−1.3%. This discrepancy may derive from the amount of water. During the crystallization process from amorphous manganese oxide to α-MnO_2 and subsequent crystal growth along the *c*-axis direction, the presence of an adequate amount of water is crucial. Although the high dielectric constant of EtOH contributes to an overall reduction in the particle size, the presence of sufficient water in the reaction solution may have promoted crystal growth along the *c*-axis direction. From the above discussions, the mechanism of this nanoparticulation can derive from the reduced amount of water in the reaction solution; the crystal growth of α-MnO_2 via the dissolution/recrystallization process is successfully suppressed.

In addition to the crystallite size, the lattice constants also changed as shown in Figure S4 and Table S1 (Supporting Information). The lattice constants *a* and *c* increase as the particles become nanoparticles; the trend in *c* has a threshold of crystallite size. This is possibly due to the increase in the surface region of the particles, which have O defect regions and lower valence of Mn. The lower valence of Mn forces lattice expansion compared to the bulk, leading to an increase in the bulk lattice parameters. **Figure** 4a, Figures S5 and S6 (Supporting Information) display the Mn valence state of α-MnO_2 as determined by X-ray absorption spectroscopy (XAS)[31] and X-ray photoelectron spectroscopy (XPS) analyses, respectively. As the particle size decreases, the Mn valence state decreases as well, evinced by both the Mn *K*-edge X-ray absorption near edge structure (XANES) and the Mn 2*p* XPS spectra, as evinced by lower energy shifts. Figure 4b shows the relative amount of NH_4^+ cation in the tunnel of α-MnO_2, estimated from CHN and inductively coupled plasma atomic emission spectroscopy (ICP-AES) elemental analyses. The NH_4^+/Mn ratio of 0.108 for α-MnO_2-hydro aligns with previous research findings.[10c,32] As the particle size decreases, the NH_4^+/Mn ratio decreases. These results imply that despite the reduced NH_4^+ content inside the tunnel, the Mn valence state becomes smaller, suggesting the formation of oxygen vacancies. The O 1*s* XPS spectra (Figure 4c) show larger peaks (≈532 eV) for α-MnO_2-*i*-PrOH-2.4% and −1.3% compared to α-MnO_2-hydro, supporting the presence of oxygen defects. In addition, electron paramagnetic resonance (EPR) spectra of α-MnO_2-*i*-PrOH−1.3% (Figure S7, Supporting Information) confirm the presence of oxygen defect since the single width (ΔB) has a positive correlation with the amount of oxygen defect.[33] These findings are summarized in Figure 4d. Ultrasmall α-MnO_2 exhibits a large surface area, which is associated with oxygen vacancies, lower NH_4^+ content, and a lower Mn valence state.

Furthermore, highly porous α-MnO_2 nanoparticles are obtained using tetrabutyl ammonium (TBA) permanganate salt instead of $NaMnO_4$, as shown in Figure S6 (Supporting Information). Such organic ammonium cations are introduced into a layered MnO_2 precursor to form mesoporous structures.[34] Both α-MnO_2-*i*-PrOH-2.4% and −1.3% synthesized using $TBAMnO_4$ exhibited broader XRD patterns and smaller primary particles according to TEM images compared to those synthesized with $NaMnO_4$. Notably, α-MnO_2-*i*-PrOH-2.4% synthesized with $TBAMnO_4$ (Figure S8c, Supporting Information) has a smaller aspect ratio particle compared to that synthesized with $NaMnO_4$ (Figure 3b). The SSAs of α-MnO_2-*i*-PrOH−1.3% is 263 $m^2\ g^{-1}$, a larger value compared to that synthesized from $NaMnO_4$.

2.2. Electrochemical Multivalent-Ion Intercalation Hosts

Ultrasmall α-MnO_2 (α-MnO_2-*i*-PrOH-2.4% and −1.3%) exhibits superior cathode performances to hydrothermally synthesized α-MnO_2 (α-MnO_2-hydro) in multivalent (Zn, Mg, and Ca) battery

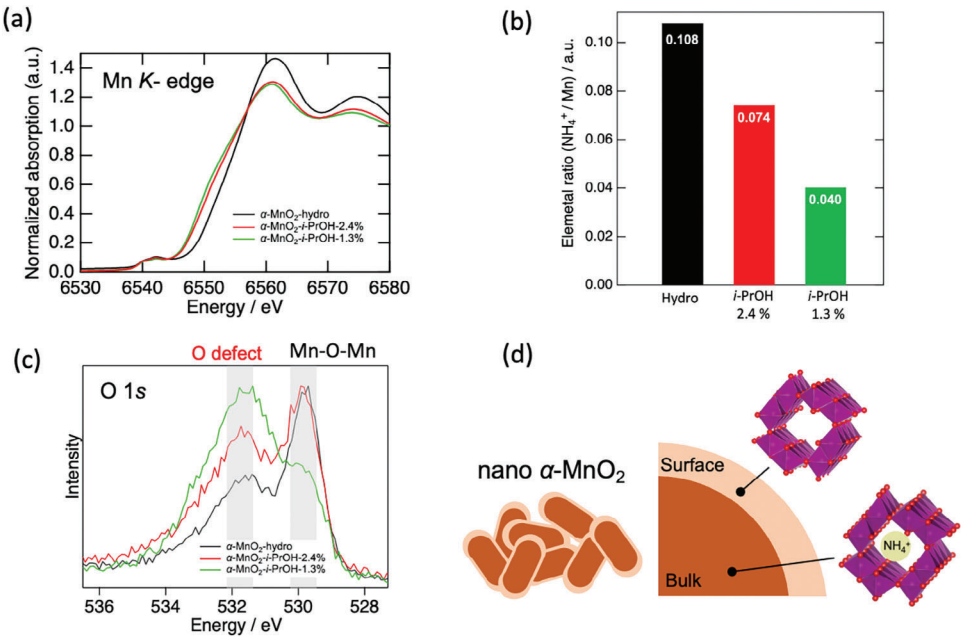

Figure 4. a) Mn *K*-edge XANES spectra. b) NH_4^+/Mn ratio calculated by CHN and ICP-AES elemental analysis. c) O 1s XPS spectra. d) Illustration of nanosized α-MnO_2 surface and bulk.

full-cells (**Figure 5**), indicating that nanoparticulation of the active material reduces multivalent ion diffusion distance, thereby enhancing cathode performance without being hindered by the sluggish diffusion of multivalent ion.

Aqueous Zn-battery, using a 1.0 M $ZnSO_4$ + 0.05 M $MnSO_4$ electrolyte, is more easily cyclable compared with nonaqueous batteries. Even at the 50th cycle (Figure 5a), α-MnO_2-*i*-PrOH-2.4% achieved the discharge capacity of more than one electron reaction (308 mAh g^{-1}) with a clear discharge plateau at ≈1.3 V attributable to Zn^{2+} intercalation,[20a] significantly improved compared with α-MnO_2-hydro. Note that the cathode performance of α-MnO_2-*i*-PrOH−1.3% was lower than α-MnO_2-*i*-PrOH-2.4%, despite its smaller particle size. It is probably due to a strong particle aggregation, especially occurring in ultrasmall nanoparticles.[35] Such aggregation increases the resistance of multivalent ion migration between particles as the interfacial resistance of α-MnO_2-*i*-PrOH−1.3% is large as shown in EIS spectra in Figure S9 (Supporting Information), resulting in inferior cathode properties, which is also a similar trend with nanosized-$LiCoO_2$ for Li-ion battery case.[36] Therefore, α-MnO_2 with smaller particle size without severe aggregation is suitable for multivalent ion battery cathodes as illustrated Figure S10 (Supporting Information). α-MnO_2-*i*-PrOH-2.4% holds a higher capacity compared with previous works[37,38] and a high-capacity retention rate of ≈100 cycles (Figure S11, Supporting Information), while α-MnO_2-hydro and α-MnO_2-*i*-PrOH−1.3% exhibit capacity degradation. Furthermore, as Figure 5b shows, α-MnO_2-*i*-PrOH-2.4% exhibits superior rate performance; even at 1 A g^{-1}, it exhibits a reversible capacity of ≈150 mAh g^{-1}. In addition, the nanosizing effect positively influences the liquid-solid reaction involving dissolved Mn^{2+}, as reported in a previous study.[39] After discharge, Mn^{2+} readily dissolves into the electrolyte and returns to the α-MnO_2 core during charging, accompanied by the formation of $ZnMn_2O_4$ on the core surface. This indicates that the cathodic performance, driven by H^+ and Zn^{2+} co-intercalation as well as the liquid-solid reaction involving dissolved Mn^{2+}, is strongly dependent on the size of the α-MnO_2 core.

In nonaqueous Mg-battery, using a 0.3 M $Mg[B(HFIP)_4]_2$ electroylte (HFIP: hexafluoroisopropyl),[40] nanosized α-MnO_2 also exhibits higher discharge capacity and cyclability (Figure 5c,d; Figure S12, Supporting Information), indicating that nanoparticulation of the active material reduces Mg^{2+} diffusion distance, thereby enhancing cathode performance without being hindered by the sluggish diffusion rate of Mg^{2+}.Moreover, galvanostatic intermittent titration technique (GITT) measurements (Figure S13, Supporting Information) exhibit that α-MnO_2-*i*-PrOH-2.4% has the smallest overvoltage at discharge.

To evaluate the impact of oxygen defects on charge/discharge performance, EPR spectra of α-MnO_2 were measured before and after annealing at 300 °C. The annealed sample of α-MnO_2-*i*-PrOH−1.3% exhibited a greater ΔB in the EPR spectra, indicating an increased amount of oxygen defects (Figure S14a, Supporting Information). This observation aligns with the previous report.[41] When comparing the voltage profiles of α-MnO_2-*i*-PrOH-2.4%, which demonstrated the best cathodic performance, with its annealed counterpart, the cathodic performance significantly deteriorated after annealing. The annealed sample showed a lower operating voltage and reduced discharge capacity, attributed to a higher concentration of oxygen defects. These defects impair the structural stability required for Mg-ion insertion, reducing structural tolerance. We estimate that the increased oxygen defects accelerate the phase transition from the hollandite structure to the halite phase, resulting in diminished capacity and a lower operating voltage. Note that there is no significant change in its specific surface area before and after annealing; annealed

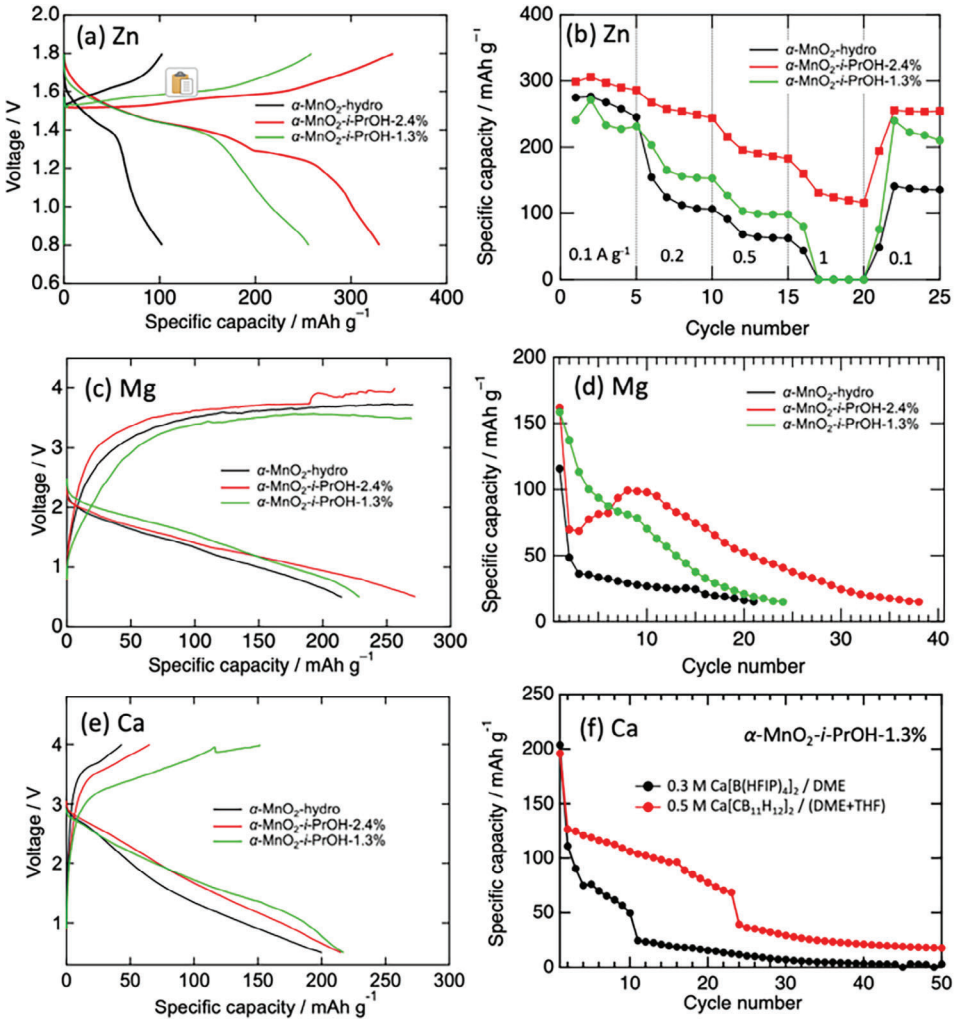

Figure 5. a) 50th-cycled voltage profile of Zn-battery cell at a current density of 100 mA g^{-1}). b) Rate capability of Zn-battery cell. c) 1st voltage profile of Mg-battery cell at a current density of 10 mA g^{-1}. d) Discharge capacity of Mg-battery cell during cycles at a current density of 100 mA g^{-1}. e) 1st voltage profile of Ca-battery cell at a current density of 10 mA g^{-1}. f) Discharge capacity of Ca-battery cell with different electrolytes during cycles at a current density of 100 mA g^{-1}.

α-MnO_2-*i*-PrOH-2.4% possess 122 m^2 g^{-1}. Despite optimizing α-MnO_2 particle size, controlling aggregation and changing the amount of oxygen defect, degradation occurred during cycling. According to the recent density functional theory (DFT) calculations, the insertion of Mg ions into α-MnO_2 distorts the tunnel structure from square to rhombus.[42] Consistently, *ex-situ* XRD measurements of α-MnO_2-hydro, exhibiting the most severe cycle degradation, revealed a broadening of the 310-plane peak after discharge, failing to revert to its pristine state (Figure S15, Supporting Information). This observation suggests the entrapment of Mg^{2+} ions within the tunnel structure, impeding their deintercalation during charging, consequently leading to capacity degradation. Thus, even with optimized particle conditions as in α-MnO_2-*i*-PrOH-2.4%, complete deintercalation of Mg ions remains a challenge.

For nonaqueous Ca-battery cell tests as shown in Figure 5e, α-MnO_2-*i*-PrOH-2.4% and −1.3% demonstrate superior cathodic performance, as well as the Mg-battery cell using a $B(HFIP)_4$-based electrolyte,[43] primarily due to the reduction in the diffusion distance of Ca^{2+}. On the contrary to the Mg and Zn-battery cases, α-MnO_2-*i*-PrOH−1.3% exhibits a larger charge capacity, suggesting that nanoparticulation may contribute rather to charge performance, specifically in Ca^{2+} deintercalation.

Furthermore, upon comparing the voltage profiles at 10 mA g^{-1} and 100 mA g^{-1}, there appears to be no significant deviation in capacity and polarization between discharge and charge (Figure S16, Supporting Information), implying that Ca^{2+} undergo intercalation and de-intercalation more rapidly than Mg^{2+}, possibly due to differences in their charge density.

Concerning the cyclability of α-MnO_2-*i*-PrOH−1.3% in the Ca-battery system, assessing its cathode performance with $Ca[B(HFIP)_4]_2$ electrolyte presents challenges due to the formation of a CaF_2 passivation layer on Ca metal,[44] resulting in substantial cycle degradation. To address this issue, a Ca full-cell test using $Ca[CB_{11}H_{12}]_2$ electrolyte was conducted; a fluorine-free electrolyte having high anodic stability (>4 V vs Ca^{2+}/Ca).[45]

As shown in Figure 5f and Figure S17 (Supporting Information), $Ca[CB_{11}H_{12}]_2$ electrolyte notably enhances the cyclability of the cathode compared with $Ca[B(HFIP)_4]_2$ electrolyte, suggesting that most cycle degradation stems from anodic issues and α-MnO_2-*i*-PrOH−1.3% was found to be superior host material for Ca-battery. Note that the coulombic efficiency of $Ca[CB_{11}H_{12}]_2$ electrolyte is ≈84% and the passivation layer, which is mainly CaH_2, is gradually formed. This is the main reason for capacity degradation shown Figure 5f. In addition, the coulombic efficiency in the first cycle was far from ideal even with using an F-free electrolyte. Figure S18 (Supporting Information) presents the XRD patterns of α-MnO_2-*i*-PrOH−1.3% after discharge and charge. Even though DFT calculation expect no structural distortion for Ca^{2+} insertion, the 310 peak shifted to a lower angle, indicating its structural change and Ca ions were trapped within the structure. Then, this causes low coulombic efficiency in the first cycle and the charge capacity is significantly dependent on the particle size, suggesting that the short migration path facilitate the Ca ion de-insertion.

In charge-discharge reactions using organic electrolytes such as Ca- and Mg-battery, in addition to cation insertion reactions, side reactions such as electrolyte reductive decomposition reactions[46] and O^{2-} release[47] are likely to occur, hence the contribution ratio of cation insertion to capacity is important. Scanning electron microscopy (SEM)-energy dispersive X-ray spectroscopy (EDX) analyses were applied to quantify the cation insertion levels. Figure S19 (Supporting Information) presents the ratio of Mg^{2+} and Ca^{2+} intercalation reaction per whole discharge reaction. Concerning Mg^{2+} intercalation ability, α-MnO_2-*i*-PrOH-2.4% exhibits the highest Mg^{2+} contribution of 78% to discharge capacity; more than 20% of side reactions occur. In particular, only 60% of capacity is contributed by Mg^{2+} insertion in the case of α-MnO_2-*i*-PrOH−1.3%. In contrast, Ca^{2+} intercalation rather proceeds in all α-MnO_2 cathodes. Particularly noteworthy is α-MnO_2-*i*-PrOH−1.3%, showing a remarkable 91% cation contribution to capacity. Moreover, α-MnO_2-*i*-PrOH−1.3% shows excellent selectivity in both Ca^{2+} intercalation and de-intercalation reactions. As displayed in Table S3 (Supporting Information), almost all charging capacity stems from Ca^{2+} de-intercalation, highlighting the superior performance of nanosized α-MnO_2 as a host material for Ca^{2+} at room temperature compared to Mg^{2+}. This host performance owes not only to the low charge density of Ca^{2+} and facile diffusion through its solid phase but also to previous DFT calculations[48] indicating that Ca^{2+} insertions cause minimal distortion to the tunnel structure of α-MnO_2. Additionally, as shown in Figure S20 (Supporting Information), Mn *K*-edge XANES analysis, tracing the redox reactions of Mn during the intercalation and deintercalation of Ca ions, indicates semi-reversible redox processes, consistent with the observed voltage profile in the first cycle. Notably, compared with spectra of other samples, α-MnO_2-*i*-PrOH−1.3% possess the highest Mn re-oxidation ability.

As discussed above, α-MnO_2-*i*-PrOH−1.3% exhibits excellent properties as a Ca-battery cathode. However, there is still potential for further performance improvement. As shown in the TEM images (Figure 3c; Figure S1f, Supporting Information), the primary particles are strongly aggregated. Additionally, electrochemical impedance spectroscopy (EIS) data presented in Figure S21 (Supporting Information) indicated a large cathodic interfacial resistance for α-MnO_2-*i*-PrOH−1.3%. This aggregation thereby causing the lack of conductivity likely contributes to the reduced performance. To address this issue, we aimed to suppress particle aggregation by compositing nanoparticles with some porous dispersant materials. Since the alcohol solution process is a wet process, the composite is easily obtained by mixing dispersant into the solution. Here we selected conductive graphene nanosheets. **Figure 6**a displays HR-TEM images of the α-MnO_2-*i*-PrOH−1.3%-graphene composite, denoted as α-MnO_2-*i*-PrOH−1.3%-G. The primary α-MnO_2 nanoparticles were homogeneously dispersed on the graphene sheet, and particle aggregation was scarcely observed. The SAED patterns (Figure 6b) and XRD patterns (Figure S22, Supporting Information) show diffraction rings corresponding to the XRD patterns, confirming the crystalline phases of α-MnO_2 and graphene. Regarding its cathodic performance in Ca-battery tests (Figure 6c), α-MnO_2-*i*-PrOH−1.3%-G exhibited significantly superior charge-discharge performance, especially in the charge curve. The polarization at 150 mAh g^{-1} was reduced from 2.60 V to 1.87 V, achieving the fully reversible charge. When comparing the polarization of nanosized α-MnO_2-graphene composite cathodes with different particle sizes and aspect ratios, the most significant reduction in polarization was observed with the α-MnO_2-*i*-PrOH−1.3% cathode (Figure 6d). This implies that the graphene composite is a highly effective method for fully utilizing the strongly aggregated nanoparticles as cathodes. As shown in Figure S23 (Supporting Information), its capacity degradation at first few cycles was significantly suppressed by compositing with graphene.

2.3. Aerobic Oxidation Catalysis

In general, it is known that the catalytic activity increases with decreasing the SSA of manganese oxides, but there is no detailed discussion on how the aspect ratio of α-MnO_2 affects the catalytic performance for the oxidation reactions. Firstly, the catalytic activities of three manganese oxide catalysts prepared in this study, α-MnO_2-hydro, α-MnO_2-*i*-PrOH-2.4%, and α-MnO_2-*i*-PrOH−1.3%, were compared for the oxidation of 1-phenylethanol (secondary alcohol) to acetophenone using O_2 as a model reaction. **Figure 7**a shows the reaction profiles, where the order of the catalytic activities was α-MnO_2-hydro < α-MnO_2-*i*-PrOH-2.4% < α-MnO_2-*i*-PrOH−1.3%. In all cases, the reactions proceeded selectively, and no byproducts other than acetophenone were detected. The initial reaction rates determined at less than 10% 1-phenylethanol conversion were 1.25 mM min^{-1}, at 2.21 mM min^{-1}, and 3.05 mM min^{-1} for α-MnO_2-hydro, α-MnO_2-*i*-PrOH-2.4%, and α-MnO_2-*i*-PrOH−1.3%, respectively, and the relationship between initial reaction rates and the SSAs was found to be a nearly first order (Table S2, Supporting Information). This means that the oxidation of 1-phenylethanol by α-MnO_2 (in other words, the reduction of α-MnO_2) can be considered to depend simply on just their SSA, without regard to the aspect ratios. However, comparing the reaction profiles of α-MnO_2-hydro and α-MnO_2-*i*-PrOH−1.3%, for example, a clear difference can be observed in the latter half of the reaction that cannot be explained by the difference in their SSAs alone. This result is considered to be due to the fact that more c planes are exposed in the

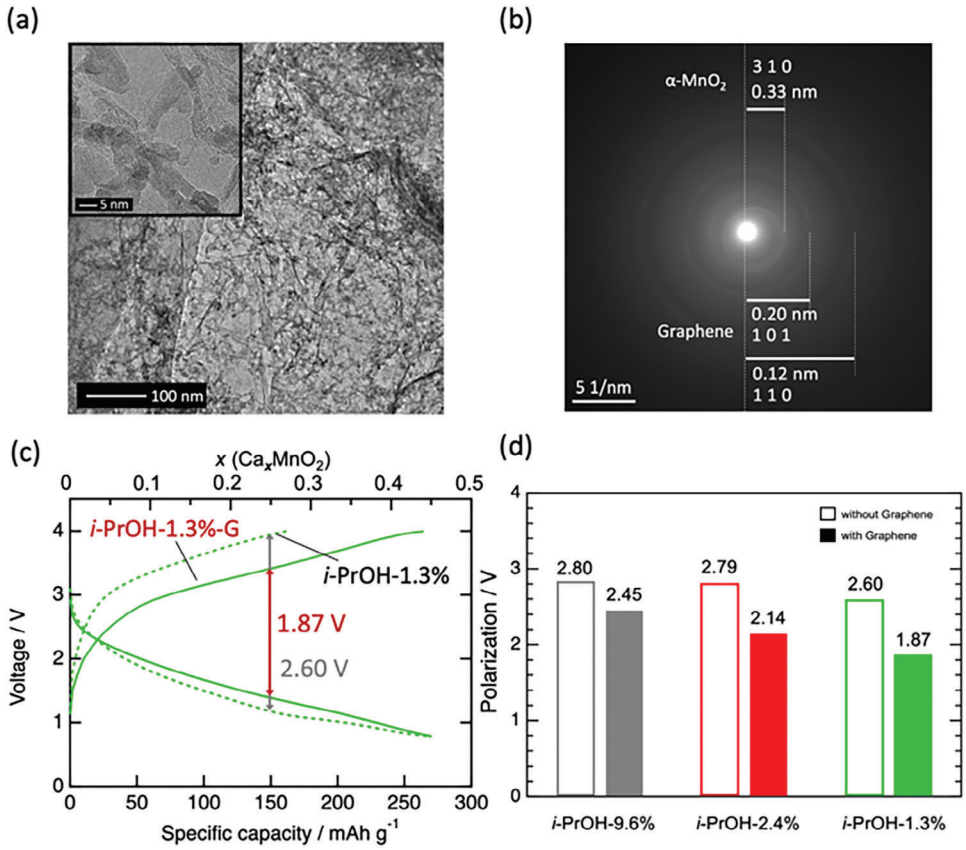

Figure 6. a) HR-TEM images and b) SAED patterns of α-MnO_2-*i*-PrOH−1.3%-G. c) Voltage profiles of Ca-battery cell at a current density of 100 mA g^{-1} and d) polarizations at the point of 150 mAh g^{-1}.

case of α-MnO_2 with a low aspect ratio (c/a), where electron transfer from the reduced manganese species to O_2 proceeds smoothly to complete the catalytic cycle. Based on these results, designing α-MnO_2 with a small SSA and small aspect ratio (c/a) is a very effective strategy for oxidation reactions of this type of substrate.

Finally, the substrate scope of ultrasmall α-MnO_2 catalysts to various oxidation reactions was investigated. With ultrasmall α-MnO_2 catalysts, the selective oxidation of not only secondary alcohols but also primary alcohols to aldehydes proceeded efficiently. The reaction of benzyl alcohol with α-MnO_2-

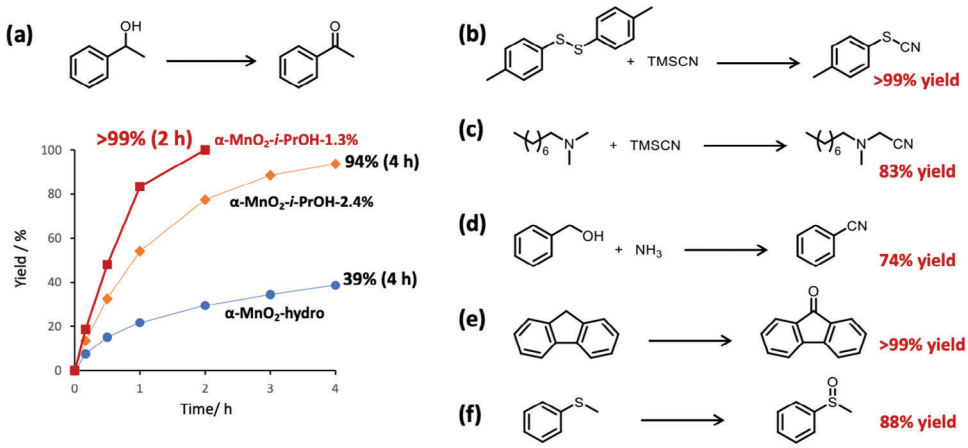

Figure 7. α-MnO_2-catalyzed aerobic oxidations of a) 1-phenylethanol, b) benzyl alcohol, c) di-*p*-tolyl disulfide, d) *N*,*N*-dimethyl octylamine, e) fluorene, and f) thioanisole. Reaction conditions were described in the experimental section. For the reactions (b–f), α-MnO_2-*i*-PrOH−1.3% was used as a catalyst. In reactions (b), (c), and (f), benzamide (25% yield), methylene cyanated product (11% yield), and methyl phenyl sulfone (5% yield) formed as byproducts, respectively.

i-PrOH−1.3% as a catalyst in the presence of NH_3 gave benzonitrile in 74% yield for 30 min (Figure 7b); this reaction consists of oxidation of benzyl alcohol to benzaldehyde, the reaction of benzaldehyde with NH_3 to form an aldimine, followed by the oxidation to the corresponding nitrile. In this case, benzamide was also formed in 25% by nitrile hydration.[49] When the reaction of benzyl alcohol with α-MnO_2-*i*-PrOH-2.4% (otherwise conditions were the same) was carried out for 1 h, the selectivity switch occurred to afford benzamide in 93% yield. α-MnO_2-*i*-PrOH−1.3% was also extremely effective for reactions originating from SET oxidation (Figure 7c,d). In the reaction of a disulfide, a thiol and target thiocyanate were first formed by the nucleophilic addition of CN^- to the disulfide substrate, but α-MnO_2-*i*-PrOH−1.3% showed extremely high catalytic activity for thiol homocoupling via SET oxidation, resulting in selective production of the thiocyanate product (Figure 7c). The α-methyl-selective oxidative cyanation was achieved through the α-MnO_2-*i*-PrOH−1.3%-mediated SET/deprotonation/SET sequence followed by the nucleophilic addition of CN^- (Figure 7d). Moreover, α-MnO_2-*i*-PrOH−1.3% was effective for the oxygenation reactions of various substrates such as alkylarenes (Figure 7e) and sulfides (Figure 7f).

3. Conclusion

Ultrasmall α-MnO_2 (<10 nm) with a low aspect ratio ($c/a \approx 2$) was, for the first time, successfully synthesized using an alcohol solution process, without any metal doping. Its potential as a host material for multivalent ion (Mg^{2+}, Ca^{2+}, and Zn^{2+}) battery cathodes and as an aerobic oxidation catalyst was fully demonstrated. In the realm of battery application, ultrasmall α-MnO_2 demonstrates superior cathodic performance compared to conventional-sized counterparts in all the battery systems, primarily due to the significant reduction in cation diffusion distance within the solid structure. In particular, ultrasmall α-MnO_2 homogeneously dispersed onto graphene nanosheets was found to be a promising cathode material for Ca-battery. Regarding aerobic oxidation catalysis, the impact of nanosizing is profound, leading to a substantial increase in the efficiency of oxidative conversion reactions of various molecules, such as 1-phenylethanol oxidation, attributable to the vastly expanded active surface area of the catalyst. Thus, the ultrasmall α-MnO_2 has made a significant impact not only in the field of batteries but also in catalysis. It can be anticipated that this material will not only find applications in next-generation green energy technologies but also set new standards for technologies across various industrial sectors.[27,29,30]

Acknowledgements

Parts of this work were supported by JSPS KAKENHI (23K13816), JST ALCA-SPRING (JPMJAL1301), JST GteX (JPMJGX23S1), Cooperative Research Program of NJRC Mater. & Dev. (MEXT), Power Academy, the Light Metal Educational Foundation, and International Joint Graduate Program in Materials Science: GP-MS at Tohoku University, Japan. This work contributes to the research performed at CELEST (Center for Electrochemical Energy Storage Ulm-Karlsruhe) and was partly funded by the German Research Foundation (DFG) under Project ID 390874152 (POLiS Cluster of Excellence).

Conflict of Interest

The authors declare no conflict of interest.

Author Contributions

H.K. conceptualized the idea for the study. H.K. designed the methodology. R.I. (lead) and H.K. performed formal analysis. R.I. (synthesis, Mg and Zn battery), S.K. (synthesis, Ca battery), T.Y. (Zn battery), S.T. (Zn battery), K.Y. (catalyst), N.K. (PDF) performed investigation. T.M. (Mg electrolyte) and K.K. (Ca electrolyte) acquired resources. R.I. wrote the original draft. H.K. (lead), K.Y., T.M., K.K., N.K., Z.Z.-K., S.O., Y.I., M.M., M.F., I.H., and T.I. wrote, reviewed, and edited the manuscript. Z.Z.-K., S.O., Y.I., M.M., M.F., I.H, and T.I. performed supervision. H.K. performed project administration. H.K. performed funding acquisition.

Data Availability Statement

The data that support the findings of this study are available from the corresponding author upon reasonable request.

Keywords

catalyst, cathode, manganese oxide, nanoparticle

[1] R. Yang, Y. Fan, R. Ye, Y. Tang, X. Cao, Z. Yin, Z. Zeng, *Adv. Mater.* **2021**, *33*, 2004862.

[2] I. Kruk, P. Zajdel, W. van Beek, I. Bakaimi, A. Lappas, C. Stock, M. A. Green, *J. Am. Chem. Soc.* **2011**, *133*, 13950.

[3] a) Q. Feng, H. Kanoh, K. Ooi, *J. Mater. Chem.* **1999**, *9*, 319; b) C. Sun, Y. Zhang, S. Song, D. Xue, *J. Appl. Cryst.* **2013**, *46*, 1128; c) D. M. Robinson, Y. B. Go, M. Mui, G. Gardner, Z. Zhang, D. Mastrogiovanni, E. Garfunkel, J. Li, M. Greenblatt, G. C. Dismukes, *J. Am. Chem. Soc.* **2013**, *135*, 3494; d) T. Hatakeyama, H. Li, N. L. Okamoto, K. Shimokawa, T. Kawaguchi, H. Tanimura, S. Imashuku, M. Fichtner, T. Ichitsubo, *Chem. Mater.* **2021**, *33*, 6983; e) W. Zhao, S. J. B. Rubio, Y. Dang, S. L. Suib, *ACS ES&T Eng.* **2022**, *2*, 20.

[4] a) J. Luo, H. T. Zhu, H. M. Fan, J. K. Liang, H. L. Shi, G. H. Rao, J. B. Li, Z. M. Du, Z. X. Shen, *J. Phys. Chem. C* **2008**, *112*, 12594; b) Y. Yuan, A. Nie, G. M. Odegard, R. Xu, D. Zhou, S. Santhanagopalan, K. He, H. Asayesh-Ardakani, D. D. Meng, R. F. Klie, C. Johnson, J. Lu, R. Shahbazian-Yassar, *Nano Lett.* **2015**, *15*, 2998.

[5] a) D. Zheng, S. Sun, W. Fan, H. Yu, C. Fan, G. Cao, Z. Yin, X. Song, *J. Phys. Chem. B* **2005**, *109*, 16439; b) Y. Dong, H. Yang, K. He, S. Song, A. Zhang, *Appl. Catal. B* **2009**, *85*, 155.

[6] a) M. M. Thackeray, M. H. Rossouw, R. J. Gummow, D. C. Liles, K. Pearce, A. De Kock, W. I. F. David, S. Hull, *Electrochim. Acta* **1993**, *38*, 1259; b) P. K. Gupta, A. Bhandari, J. Bhattacharya, R. G. S. Pala, *J. Phys. Chem. C* **2018**, *122*, 11689.

[7] a) Y. Chabre, J. Pannetier, *Prog. Solid State Chem.* **1995**, *23*, 1; b) S. Chou, F. Cheng, J. Chen, *J. Power Sources* **2006**, *162*, 727.

[8] a) C. A. J. Appelo, D. Postma, *Geochim. Cosmochim. Acta* **1999**, *63*, 3039; b) J. Zhou, L. Yu, M. Sun, S. Yang, F. Ye, J. He, Z. Hao, *Ind. Eng. Chem. Res.* **2013**, *52*, 9586.

[9] a) J. C. Hunter, *J. Solid. State Chem.* **1981**, *39*, 142; b) J. E. Greedan, N. P. Raju, A. S. Wills, C. Morin, S. M. Shaw, J. N. Reimers, *Chem. Mater.* **1998**, *10*, 3058.

[10] a) D. A. Tompsett, M. S. Islam, *Chem. Mater.* **2013**, *25*, 2515; b) C. Ling, R. Zhang, F. Mizuno, *ACS Appl. Mater. Interfaces* **2016**, *8*, 4508; c) L. M. Housel, L. Wang, A. Abraham, J. Huang, G. D. Renderos, C. D. Quilty, A. B. Brady, A. C. Marschilok, K. J. Takeuchi, E. S. Takeuchi, *Acc. Chem. Res.* **2018**, *51*, 575; d) J. Fu, X. Luo, *RSC Adv.* **2020**, *10*, 39895; e) X. Gao, H. Wu, W. Li, Y. Tian, Y. Zhang, H. Wu, L. Yang, G. Zou, H. Hou, X. Ji, *Small* **2020**, *16*, 1905842.

[11] a) T. Uematsu, Y. Miyamoto, Y. Ogasawara, K. Suzuki, K. Yamaguchi, N. Mizuno, *Catal. Sci. Technol.* **2016**, *6*, 222; b) E. Hayashi, Y. Yamaguchi, K. Kamata, N. Tsunoda, Y. Kumagai, F. Oba, M. Hara, *J. Am. Chem. Soc.* **2019**, *141*, 890.

[12] a) A. Umar, A. A. Ibrahim, R. Kumar, H. Albargi, W. Zeng, M. A. M. Alhmami, M. A. Alsaiari, S. Baskoutas, *Mater. Lett.* **2021**, *286*, 129232; b) C. Revathi, R. T. R. Kumar, *Electroanalysis* **2017**, *29*, 1481.

[13] a) H. Li, L. Gui, Z. Gao, F. Ren, H. Zhang, R. Peng, *Nanotechnology* **2021**, *32*, 215705; b) M. A. El-Ghobashy, I. A. Salem, W. M. El-Dahrawy, M. A. Salem, *J. Mol. Struct.* **2023**, *1272*, 134118.

[14] a) L. I. Hill, R. Portal, A. Verbaere, D. Guyomard, *Electrochem. Solid-State Lett.* **2001**, *4*, A180; b) J. Huang, A. S. Poyraz, S.-Y. Lee, L. Wu, Y. Zhu, A. C. Marschilok, K. J. Takeuchi, E. S. Takeuchi, *ACS Appl. Mater. Interfaces* **2017**, *9*, 4333; c) X. Wang, F. Zhang, C. Xia, L. Cui, F. Yang, *J. Alloys Compd.* **2024**, *970*, 172599.

[15] A. B. Brady, K. R. Tallman, E. S. Takeuchi, A. C. Marschilok, K. J. Takeuchi, P. Liu, *J. Phys. Chem. C* **2019**, *123*, 25042.

[16] a) N. Tang, X. Tian, C. Yang, Z. Pi, Q. Han, *J. Phys. Chem. Solids* **2010**, *71*, 258; b) Y. Sun, S. Wang, Y. Dai, X. Lei, *Funct. Mater. Lett.* **2015**, *09*, 1650005.

[17] a) R. Zhang, X. Yu, K.-W. Nam, C. Ling, T. S. Arthur, W. Song, A. M. Knapp, S. N. Ehrlich, X.-Q. Yang, M. Matsui, *Electrochem. Commun.* **2012**, *23*, 110; b) B. Wu, G. Zhang, M. Yan, T. Xiong, P. He, L. He, X. Xu, L. Mai, *Small* **2018**, *14*, 1703850; c) C. Zuo, F. Xiong, J. Wang, Y. An, L. Zhang, Q. An, *Adv. Funct. Mater.* **2022**, *32*, 2202975; d) Y. Qi, H. Li, K. Shimokawa, X. Ye, T. Kawaguchi, T. Ichitsubo, *J. Phys. Chem. C* **2023**, *127*, 21271; e) K. Shimokawa, T. Hatakeyama, H. Li, T. Ichitsubo, *Curr. Opin. Electrochem.* **2023**, *38*, 101209.

[18] W. Zhang, H. Li, Z. Zhang, M. Xu, Y. Lai, S.-L. Chou, *Small* **2020**, *16*, 2001524.

[19] Y. Tian, G. Zeng, A. Rutt, T. Shi, H. Kim, J. Wang, J. Koettgen, Y. Sun, B. Ouyang, T. Chen, Z. Lun, Z. Rong, K. Persson, G. Ceder, *Chem. Rev.* **2021**, *121*, 1623.

[20] a) T. Le, N. Sadique, L. M. Housel, A. S. Poyraz, E. S. Takeuchi, K. J. Takeuchi, A. C. Marschilok, P. Liu, *ACS Appl. Mater. Interfaces* **2021**, *13*, 59937; b) Q. Yang, Y. Chen, Y. Yang, T. Xu, Y. Lin, X. Zhang, J. Wang, Y.-N. Liu, Y. Li, *Ind. Eng. Chem. Res.* **2023**, *62*, 16757.

[21] K. Ma, Q. Li, C. Hong, G. Yang, C. Wang, *ACS Appl. Mater. Interfaces* **2021**, *13*, 55208.

[22] a) M. Koutani, E. Hayashi, K. Kamata, M. Hara, *J. Am. Chem. Soc.* **2022**, *144*, 14090; b) K. Kamata, N. Kinoshita, M. Koutani, R. Aono, E. Hayashi, M. Hara, *Catal. Sci. Technol.* **2022**, *12*, 6219.

[23] a) J.-H. Moon, H. Munakata, K. Kajihara, K. Kanamura, *Electrochemistry* **2013**, *81*, 2; b) G. Zhu, J. Zhu, W. Li, W. Yao, R. Zong, Y. Zhu, Q. Zhang, *Environ. Sci. Technol.* **2018**, *52*, 8684.

[24] a) Z. Hu, X. Xiao, C. Chen, T. Li, L. Huang, C. Zhang, J. Su, L. Miao, J. Jiang, Y. Zhang, J. Zhou, *Nano Energy* **2015**, *11*, 226; b) S. Chen, S. Zhang, T. Wang, Z. Lei, M. Zhu, X. Dai, F. Liu, J. Li, H. Yin, *Mater. Chem. Phys.* **2018**, *208*, 258; c) A. Khan, A. M. Toufiq, F. Tariq, Y. Khan, R. Hussain, N. Akhtar, S. U. Rahman, *Mater. Res. Express* **2019**, *6*, 065043; d) M. Lübke, A. Sumboja, L. McCafferty, C. F. Armer, A. D. Handoko, Y. Du, K. McColl, F. Cora, D. Brett, Z. Liu, J. A. Darr, *ChemistrySelect* **2018**, *3*, 2613; e) R. C. Korošec, P. Umek, A. Gloter, J. Padežnik Gomilšek, P. Bukovec, *Beilstein J. Nanotechnol.* **2017**, *8*, 1032; f) S. M. Alharbi, M. A. Alkhalifah, B. Howchen, A. N. A. Rahmah, V. Celorrio, D. J. Fermin, *ACS Mater. Au* **2024**, *4*, 74; g) X. Hu, J. Chen, S. Li, Y. Chen, W. Qu, Z. Ma, X. Tang, *J. Phys. Chem. C* **2020**, *124*, 701.

[25] a) H. Kobayashi, K. Yamaguchi, I. Honma, *RSC Adv.* **2019**, *9*, 36434; b) Y. Sugawara, H. Kobayashi, I. Honma, T. Yamaguchi, *ACS Omega* **2020**, *5*, 29388; c) R. Iimura, H. Watanabe, T. Mandai, I. Honma, H. Imai, H. Kobayashi, *ACS Appl. Energy Mater.* **2024**, *7*, 5308.

[26] A. Manthiram, J. Kim, S. Choi, *MRS Proc.* **1999**, *575*, 9.

[27] F. Izumi, K. Momma, *Solid State Phenom.* **2007**, *130*, 15.

[28] S. Hong, S. Jin, Y. Deng, R. Garcia-Mendez, K.-i. Kim, N. Utomo, L. A. Archer, *ACS Energy Lett.* **2023**, *8*, 1744.

[29] S. Kohara, M. Itou, K. Suzuya, Y. Inamura, Y. Sakurai, Y. Ohishi, M. Takata, *J. Phys. Condens. Matter* **2007**, *19*, 506101.

[30] D. A. Keen, *J. Appl. Cryst.* **2001**, *34*, 172.

[31] B. Ravel, M. Newville, *J. Synchrotron Rad.* **2005**, *12*, 537.

[32] C. S. Johnson, D. W. Dees, M. F. Mansuetto, M. M. Thackeray, D. R. Vissers, D. Argyriou, C. K. Loong, L. Christensen, *J. Power Sources* **1997**, *68*, 570.

[33] M. Kakazey, N. Ivanova, Y. Boldurev, S. Ivanov, G. Sokolsky, J. G. Gonzalez-Rodriguez, M. Vlasova, *J. Power Sources* **2003**, *114*, 170.

[34] J. Luo, S. L. Suib, *Chem. Commun.* **1997**, 1031.

[35] H. Kobayashi, Y. Fukumi, H. Watanabe, R. Iimura, N. Nishimura, T. Mandai, Y. Tominaga, M. Nakayama, T. Ichitsubo, I. Honma, H. Imai, *ACS Nano* **2023**, *17*, 3135.

[36] M. Okubo, E. Hosono, J. Kim, M. Enomoto, N. Kojima, T. Kudo, H. Zhou, I. Honma, *J. Am. Chem. Soc.* **2007**, *129*, 7444.

[37] Y. Chen, Z. Li, B. Li, Z. Zhang, J. Wei, B. Wang, Y. Huang, *ACS Appl. Energy Mater.* **2023**, *6*, 3329.

[38] L. Wu, Z. Li, Y. Xiang, W. Dong, X. Qi, Z. Ling, Y. Xu, H. Wu, M. D. Levi, N. Shpigel, X. Zhang, *Small* **2024**, *20*, 2404583.

[39] S. J. Kim, D. Wu, N. Sadique, C. D. Quilty, L. Wu, A. C. Marschilok, K. J. Takeuchi, E. S. Takeuchi, Y. Zhu, *Small* **2020**, *16*, 2005406.

[40] T. Mandai, *ACS Appl. Mater. Interfaces* **2020**, *12*, 39135.

[41] T. Subramaniam, B. S. Krishnaveni, S. Devaraj, *J. Mater. Sci.: Mater. Electron.* **2024**, *35*, 1184.

[42] C. Ling, R. Zhang, T. S. Arthur, F. Mizuno, *Chem. Mater.* **2015**, *27*, 5799.

[43] A. Shyamsunder, L. E. Blanc, A. Assoud, L. F. Nazar, *ACS Energy Lett.* **2019**, *4*, 2271.

[44] a) Z. Li, O. Fuhr, M. Fichtner, Z. Zhao-Karger, *Energy Environ. Sci.* **2019**, *12*, 3496; b) Z. Li, B. P. Vinayan, T. Diemant, R. J. Behm, M. Fichtner, Z. Zhao-Karger, *Small* **2020**, *16*, 2001806.

[45] a) K. Kisu, S. Kim, T. Shinohara, K. Zhao, A. Züttel, S. Orimo, *Sci. Rep.* **2021**, *11*, 7563; b) K. Kisu, R. Mohtadi, S. Orimo, *Adv. Sci.* **2023**, *10*, 2301178.

[46] a) R. Iimura, H. Kobayashi, I. Honma, *Electrochemistry* **2022**, *90*, 067002; b) J. Han, S. Yagi, H. Takeuchi, M. Nakayama, T. Ichitsubo, *J. Phys. Chem. C* **2022**, *126*, 19074; c) W. Zhou, C. Xu, B. Gao, M. Nakayama, S. Yagi, Y. Tateyama, *ACS Energy Lett.* **2023**, *8*, 4113.

[47] X. Ye, H. Li, T. Hatakeyama, H. Kobayashi, T. Mandai, N. L. Okamoto, T. Ichitsubo, *ACS Appl. Mater. Interfaces* **2022**, *14*, 56685.

[48] T. R. Juran, J. Young, M. Smeu, *J. Phys. Chem. C* **2018**, *122*, 8788.

[49] a) K. Yamaguchi, H. Kobayashi, T. Oishi, N. Mizuno, *Angew. Chem., Int. Ed.* **2012**, *51*, 544; b) K. Yamaguchi, Y. Wang, H. Kobayashi, N. Mizuno, *Chem. Lett.* **2012**, *41*, 574; c) K. Yamaguchi, H. Kobayashi, Y. Wang, T. Oishi, Y. Ogasawara, N. Mizuno, *Catal. Sci. Technol.* **2013**, *3*, 318.